Volume 9 | Number 48 | 28 December 2017 | Pages 18985–19416

Nanoscale

rsc.li/nanoscale

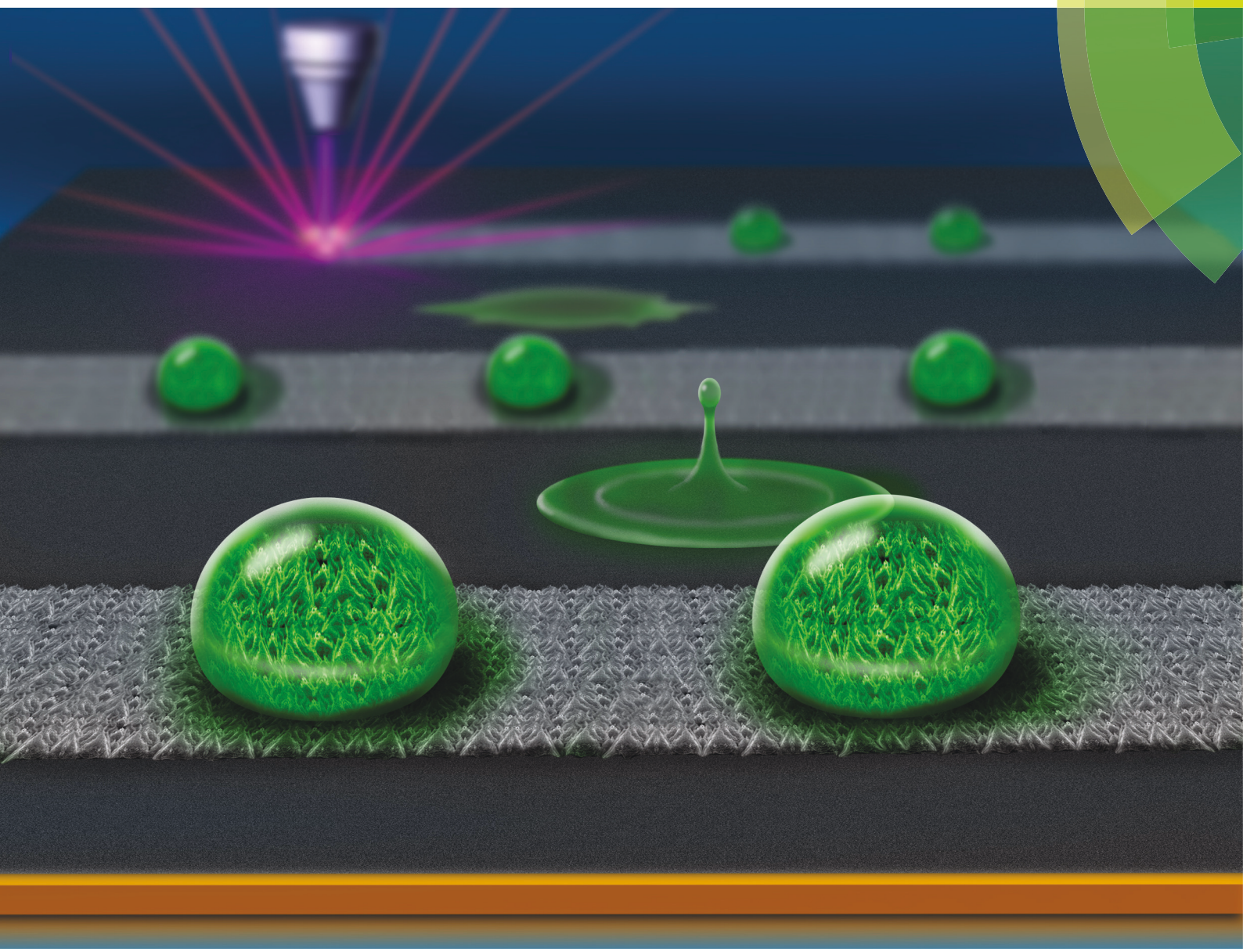

ISSN 2040-3372

ROYAL SOCIETY OF CHEMISTRY

PAPER
Jonathan C. Claussen *et al.*
Superhydrophobic inkjet printed flexible graphene circuits *via* direct-pulsed laser writing

NCNST

Nanoscale

PAPER

View Article Online
View Journal | View Issue

Cite this: *Nanoscale*, 2017, **9**, 19058

Superhydrophobic inkjet printed flexible graphene circuits *via* direct-pulsed laser writing†

Suprem R. Das, [a,b,c] Srilok Srinivasan,[a] Loreen R. Stromberg, [a] Qing He,[a] Nathaniel Garland,[a] Warren E. Straszheim,[d] Pulickel M. Ajayan,[e] Ganesh Balasubramanian[f] and Jonathan C. Claussen *[a,b,c]

Received 20th August 2017,
Accepted 29th October 2017

DOI: 10.1039/c7nr06213c

rsc.li/nanoscale

Solution-phase printing of exfoliated graphene flakes is emerging as a low-cost means to create flexible electronics for numerous applications. The electrical conductivity and electrochemical reactivity of printed graphene has been shown to improve with post-print processing methods such as thermal, photonic, and laser annealing. However, to date no reports have shown the manipulation of surface wettability *via* post-print processing of printed graphene. Herein, we demonstrate how the energy density of a direct-pulsed laser writing (DPLW) technique can be varied to tune the hydrophobicity and electrical conductivity of the inkjet-printed graphene (IPG). Experimental results demonstrate that the DPLW process can convert the IPG surface from one that is initially hydrophilic (contact angle ~47.7°) and electrically resistive (sheet resistance ~21 MΩ $\square^{-1}$) to one that is superhydrophobic (CA ~157.2°) and electrically conductive (sheet resistance ~1.1 kΩ $\square^{-1}$). Molecular dynamic (MD) simulations reveal that both the nanoscale graphene flake orientation and surface chemistry of the IPG after DPLW processing induce these changes in surface wettability. Moreover, DPLW can be performed with IPG printed on thermally and chemically sensitive substrates such as flexible paper and polymers. Hence, the developed, flexible IPG electrodes treated with DPLW could be useful for a wide range of applications such as self-cleaning, wearable, or washable electronics.

Introduction

Large-area, solution-phase printing of nanomaterials has facilitated the fabrication of low-cost, high-throughput flexible electronics for diverse applications including thin-film transistors, photovoltaics, batteries/capacitors, electronic displays, and strain/pressure sensors.[1–5] Solution-phase printing of graphene-based inks has shown promise in improving the performance of printed electronics due to graphene's favorable electrical and thermal conductivity, chemical and thermal stability, biocompatibility, and the material's natural abundance.[6,7] High-throughput printing of graphene including inkjet, gravure, flexographic, and screen printing typically requires the use of post-print annealing processes such as thermal, photonic, or laser annealing to remove binders (*e.g.*, ethyl cellulose) and solvents, sinter or weld graphene flakes together, and consequently to make the graphene sufficiently electrically conductive for various electronic and sensing applications.[8–14] Recently researchers have shown that rapid-pulse laser annealing of printed graphene can be performed on thermally and chemically sensitive materials such as paper,[8] but no post-print annealing process has focused on tuning the surface wettability or hydrophobicity of printed graphene. The formation of superhydrophobic inkjet printed graphene (IPG) that is also flexible and electrically conductive would lend enormous value to self-cleaning wearable/washable electronics that are resistant to stains, or ice and biofilm formation.[15,16]

Recent research on the hexagonal honeycomb carbon lattice in single/few layer graphene have shown that these surfaces display hydrophilic or hydrophobic properties depending on the material composition of the underlying substrate or adsorption of hydrocarbons and epoxide groups to graphene.[17,18] For example, single layer graphene creates a

[a]*Department of Mechanical Engineering, Iowa State University, Ames, IA 50011, USA. E-mail: jcclauss@iastate.edu*
[b]*Division of Materials Science and Engineering, Ames Laboratory, Ames, IA 50011, USA*
[c]*Applied Sciences Complex I and Microelectronics Research Center, Iowa State University, Ames 50011, USA*
[d]*Materials Analysis and Research Laboratory, Iowa State University, Ames, IA 50011, USA*
[e]*Department of Materials Science and Nanoengineering, Rice University, Houston, TX 77005, USA*
[f]*Department of Mechanical Engineering and Mechanics, Lehigh University, Bethlehem, PA 18015, USA*
†Electronic supplementary information (ESI) available. See DOI: 10.1039/c7nr06213c

surface that can display 'wetting transparency' in some cases, where water molecules do not effectively 'see' graphene and instead behave in accordance with the contact angle of the underlying substrate.[17,19,20] In contrast, multilayer graphene, at least four atomic layers thick, impedes wetting transparency and graphene hydrophobicity depends primarily upon superficial hydrocarbon and epoxide groups.[18,21,22] No reports have been conducted on manipulating the hydrophobicity of IPG.

Here we report the creation of IPG that is electrically conductive, mechanically robust, and superhydrophobic [contact angle (CA) > 150°] after UV-pulsed laser irradiation. Experimental results including static CA measurements and scanning electron microscopy (SEM) micrographs confirm that the wettability of the IPG transforms from one that is hydrophilic (CA ~ 47.7°) to one that is superhydrophobic (157.2°) by manipulating the energy density of the laser irradiation *via* DPLW. Micrographs and video obtained from an SEM operating in environmental mode demonstrate the formation of water droplets on hydrophilic (untreated laser regions) and not on hydrophobic (laser treated) regions. Molecular Dynamics (MD) simulations help elucidate the physiochemical underpinnings of the surface wettability and show that both the graphene flake orientation (nanopatterning) and surface chemistry induced by the direct-pulsed laser writing (DPLW) process play an important role in changing the surface wettability of the IPG.

Results and discussion

Graphene films were inkjet printed and annealed on silicon and polyimide substrates with a printed thickness of ~7 μm and post-processed *via* both DPLW and conventional thermal annealing (Fig. 1a and b). DPLW processing was conducted with increasing laser energy density (40, 70, 85, 100, and 120 mJ cm^{-2} respectively) on both the silicon and polyimide substrates. Thermal annealing was conducted with IPG on silicon substrates placed within an oven chamber filled with forming gas and heated to temperatures between 700–1000 °C. It should be noted here that the polyimide has a melting temperature of approximately 450 °C and therefore this thermal annealing process could not be performed with IPG on the polyimide substrate. Results indicated that the DPLW processing of IPG generates 3D nanostructures with features of two characteristic length scales: a local fin-like nanoscale structure (Fig. 1f), as well as a micron-scale rose-petal structure (Fig. 1d). In contrast, thermal annealing revealed a comparatively smooth surface (Fig. 1e & g).

The hydrophobicity and electrical conductivity of the IPG was significantly altered/improved by the DPLW as compared to the thermal annealing processes. Droplets of deionized water (3–6 μL, resistivity ~18.3 MΩ cm) were dispensed in several locations onto the surface, and the static CA of both DPLW and thermally treated graphene were measured *via* water contact angle goniometry (ESI,† Fig. 2 and ESI Video 1†). DPLW treated graphene displayed a sharp increase in the CA with the lowest fluence setting (125.2°, 40 mJ cm^{-2}) as compared to the control samples, Si/SiO_2 with a ~300 nm oxide layer and IPG without any annealing which yielded CAs of approximately 44.5° and 47.7° respectively. The CA for unannealed IPG was found to be consistent with that previously reported for graphene oxide (GO).[23] Note that, the developed IPG films are accompanied with oxygen functional groups.[8] DPLW operated at a laser energy density within the range of 85–100 mJ cm^{-2}, transformed the surface into one that was superhydrophobic (*i.e.*, CA > 150°). However, the IPG CA decreased (~138°) and the

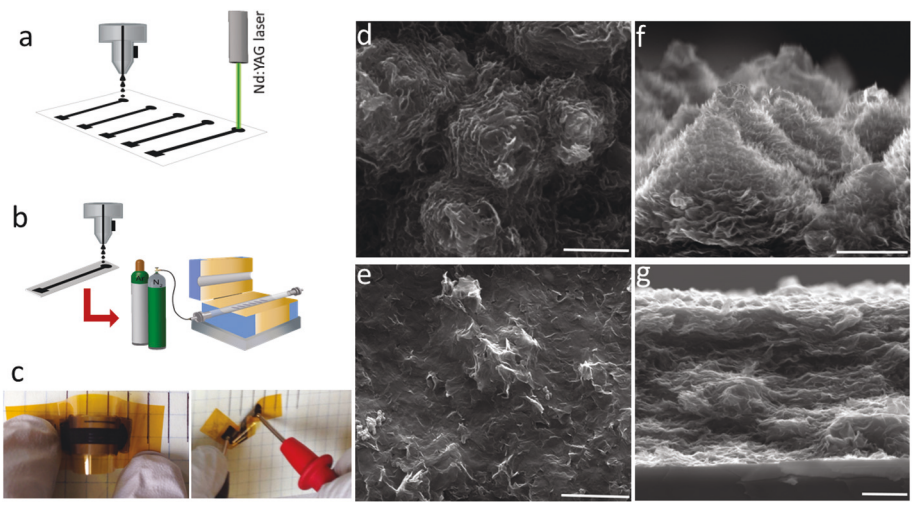

Fig. 1 Schematic diagrams portraying the inkjet printing of the reduced graphene oxide flakes as well as the post-print (a) DPLW annealing and (b) thermal annealing processing. (c) The IPG printed on polyimide withstands mechanical bending and twisting with a (left) ~2–3% and (right) 24% resistance change in each case respectively. Field emission scanning electron microscopy (FESEM) images portraying the top view of the IPG surface (d) after DPLW processing at an energy density of 100 mJ cm^{-2} and (e) after thermal annealing at a temperature of 900 °C. FESEM images portraying the cross-sectional view of the (f) DPLW processed graphene and the (g) thermally annealed graphene. All scale bars are 2 μm.

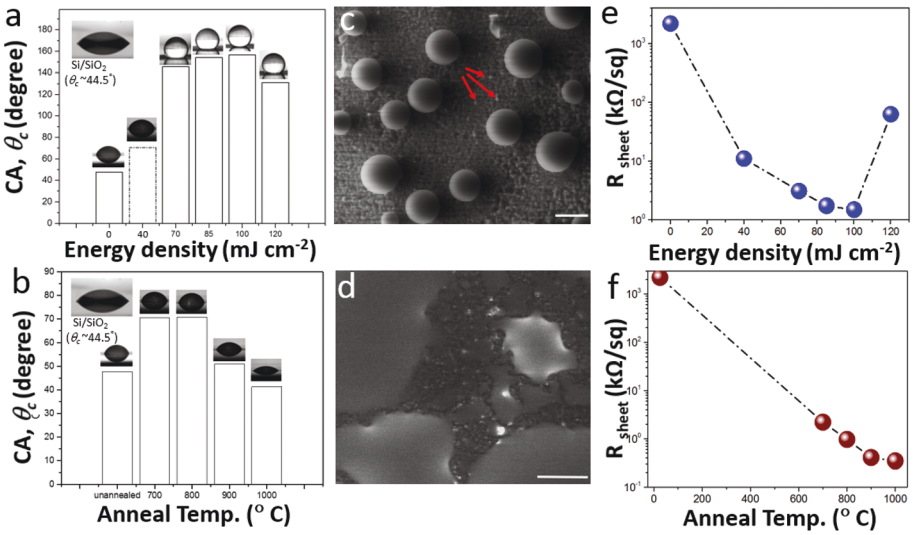

Fig. 2 Comparison of CA, condensation, and electrical sheet resistance of IPG that was DPLW annealed (a, c, e) or thermally annealed (b, d, f). (a) CAs for IPG electrodes treated with DPLW at distinct laser energy densities. (b) CAs measured on IPG that were thermally annealed at distinct temperatures. Inserts in both (a) and (b) shows the CA of a control Si/SiO_2 surface without IPG. Water condensation experiments performed on (c) laser annealed (100 mJ cm^{-2}) and (d) thermally annealed (800 °C) IPG inside an environmental SEM chamber. Scale bars correspond to 50 μm. Larger spherical droplets indicate water condensation and small bright spots (red arrows) indicate initial water droplet formation on the DPLW treated IPG. No water droplet formation was observed on the thermally annealed IPG. Electrical conductivity experiments display sheet resistance *vs.* (e) laser energy density and (f) temperature for laser and thermally annealed IPG respectively. Reported CA and sheet resistance values are reported as averages from three distinct samples (n = 3).

sample sheet resistance began to increase when laser fluence was increased to 120 mJ cm^{-2} which can be attributed to electrode degradation as the laser begins to etch/destroy the printed graphene surface at higher energy densities as previously shown.[8] The thermal annealing of IPG did not induce superhydrophobicity (maximum measured CA was 70.8°) across annealing temperatures of 800–1000 °C (Fig. 2b). Moreover, the CAs for the thermally annealed IPG were approximately 20° smaller than those obtained for multilayer (> 6 layers) and flat graphene,[17] but similar in magnitude to those reported for chemically synthesized reduced GO films.[24] The CA of thermally annealed graphene began to diminish at higher temperatures where CA values were 51.1° and 41.4° at respective annealing temperatures of 900 °C and 1000 °C. This decrease in CA at high annealing temperatures is most likely due to the smoothing of the graphene surface at higher temperatures.[7] In a similar fashion, the electrical conductivity of the distinctly annealed IPG samples changed with increasing laser energy density or annealing temperature (Fig. 2e & f). The electrical sheet resistance of the IPG samples decreased by more than three orders of magnitude from 21 MΩ $\square^{-1}$ to 1.1 kΩ $\square^{-1}$ as DPLW energy density was increased to 100 mJ cm^{-2} (Fig. 2e). It is interesting to note that 100 mJ × cm^{-2} is the same laser energy density that maximizes both the superhydrophobicity and the electrical conductivity of the IPG, ensuring the scalability of laser annealed IPG for electronics and self-cleaning applications for example. Similarly, the electrical sheet resistance of the IPG samples decreased by more than three orders of magnitude from 21 MΩ $\square^{-1}$ to 0.3 kΩ $\square^{-1}$ as the thermal annealing temperature was increased to 1000 °C (Fig. 2f). This lower sheet resistance for the thermal annealing process is most likely due to a higher sustained input energy than the rapid-pulse DPLW technique. This higher sustained input energy could lead to an increase in flake-to-flake sintering or welding and consequently to lower sheet resistances. However, thermal annealing even across the broad high-temperature range performed here (*viz.*, 700–1000 °C) is incapable of creating an IPG surface that is hydrophobic (CA ≥ 90°), let alone IPG that is superhydrophobic (CA ≥ 150°). Therefore, the subsequent simulations and experimental work focuses on analyzing DPLW treated IPG that was consequently made hydrophobic/superhydrophobic.

The surface wettability of the superhydrophobic DPLW treated (100 mJ cm^{-2}) and hydrophilic thermally annealed (800 °C) IPG were characterized *via* environmental scanning electron microscopy (ESEM) (Fig. 2c & d). Distinctly shaped, spherical water beads (dia. <5–50 μm) formed on the DPLW treated IPG during ESEM imaging (Fig. 2c). These water droplets appeared as the environmental vapor pressure, relative humidity and temperature were altered within the ESEM (see Fig. 4 discussion). Beaded water droplet formation was noticeably absent from the thermally annealed IPG during ESEM experiments (Fig. 2d)—thus further corroborating the hydrophobic and hydrophilic nature of the DPLW and thermally annealed IPG samples respectively. It should be noted that the induced superhydrophobicity is not due to wetting

transparency as GO and multi-layer graphene with thicknesses of 30 nm or greater are too thick for such phenomena.[17] Furthermore, subsequent MD simulations demonstrate that the nanoscale patterning of the graphene, *via* the laser, and subsequent contamination of the graphene with airborne hydrocarbon or epoxide adsorption help facilitate the superhydrophobic nature of the DPLW treated graphene.[18,25] Such surface contamination was noted on the DPLW treated IPG during differential scanning calorimetry (DSC) and mass spectroscopy experiments (Fig. S6 in ESI†).

To further investigate the geometric microscale origins of superhydrophobicity,[26] MD simulations were used to understand the mechanism for hydrophilic-to-hydrophobic conversion of DPLW-treated IPG. The superficial graphene CA was predicted as a function of the graphene petal orientation by modeling the molecular interactions between graphene and water. Droplet-graphene interaction energy (U_{H_2O-C}) was computed for different graphene petal orientations. The results demonstrate CA values change with the orientation of graphene flakes. However, these simulations (i) only capture the nanoscale phenomena and (ii) were performed on ordered structures, not accounting for the disorder in interlayer spacing and the petal orientation observed in the experiment. In all the simulations, the distance between the graphene layers was set to 3.4 Å based on the experimentally observed interplanar spacing in graphite.[27] We note that the spacing between graphene flakes in IPG can change after DPLW-treatment and there is a randomness associated with the petal orientation. Nevertheless, our idealized simulations help in isolating the role of petal orientation from other morphological changes due to laser treatment, and elucidates its effect on CA. The simulation domain was a 25.84 × 3.83 × 20 nm^3 box with 4000 water molecules arranged over a graphitic substrate, and equilibrated at 26.85 °C (Fig. S1 & S2 in the ESI†). The intermolecular interactions between the water molecules were described by the rigid extended simple point charge model (SPC/E)[28] and the graphene-water interactions were modeled with a 12–6 Lennard Jones potential using parameters (ε_{CO} and σ_{CO}) proposed by Werder *et al.*[29] The CA of the water droplet was determined by curve fitting a sigmoidal function (eqn (1)) over the mass density profile of the water droplet divided into sheets along the z-direction.[20,30–32]

$$\rho(r) = \frac{1}{2}(\rho_\beta(dr) + \rho_\beta(g)) - \frac{1}{2}(\rho_\beta(dr) - \rho_\beta(g))\tanh\left(\frac{2(r - r_\beta)}{d_\beta}\right) \quad (1)$$

where ρ is the mass-density, r the distance from the center of the water droplet, $\rho_\beta(dr)$ the mass density in sheet β near the center of the water droplet, $\rho_\beta(g)$ the mass density of surrounding gas (assumed to be zero), r_β the radius of the droplet in sheet β and d_β the thickness of the interface. More details regarding the mass density profile of the water droplet simulation including the use of dividing the simulation box into bins to obtain the profile are presented in the ESI (Fig. S4 & S5†). The CA (θ) is calculated as[31]

$$\theta = \lim_{\Delta z \to 0} \tan^{-1}\left(\frac{\Delta z}{r_2 - r_1}\right) \quad (2)$$

where, Δz is the thickness of each sheet.

Results from the atomistic simulations corroborate the change in CA due to local changes in the graphene petal orientation. The CAs for intermediate orientations between the horizontal and vertical positions of multi-layer graphene flakes, denoted by ϕ (angle between the plane of the graphene sheet and the positive x-axis in the horizontal direction), were calculated to further support the trend. Differences in the predicted absolute values of the CAs from the experiments are due to: (i) the system size limitation that constrains the MD analyses to only nanoscale features without including effects of microstructures observed on the samples, (ii) notable disparity in the water droplet size between experiments and simulations, and finally (iii) randomness in the petal orientation, spacing and functionalization in DPLW-treated IPG, which were not included in our model. Hence a computational scheme which can address the shortcomings of the MD model is necessary to understand the role of factors other than petal orientation.

Fig. 3a–c show the change in CA due to change in orientations of graphene and the evolution of U_{H_2O-C} with time. The CA (θ_c) of the water droplet on horizontally oriented graphene, θ_c = 76.87°, is in agreement with earlier theoretical calculations[17,20,33] and experimental measurement of CAs on exposed graphene sheets.[17,18,34] For the vertically oriented graphene sheets only arm-chair configurations of graphene edge states are considered. U_{H_2O-C} measures the interaction strength between the droplet and the substrate. U_{H_2O-C} converges $\cong -0.2$ Mcal mol^{-1} for vertically oriented graphene, while horizontally oriented graphene petals with $U_{H_2O-C} \cong -0.6$ Mcal mol^{-1} (Fig. 3c) reflect a relatively stronger attraction between the droplet and the substrate. When the adhesive interaction due to the attractive van der Waals forces between the droplet and substrate molecules overcomes the cohesive interaction between the water molecules, the surface becomes hydrophilic. Alternately, a stronger intermolecular interaction between droplet molecules relative to the adhesive forces renders the surface hydrophobic.

The horizontal configuration of few layer graphene exerts strong van der Waals attraction to the water molecules placed above given the continuous spread of carbon atoms beneath. This interaction results in a small CA and a hydrophilic surface. As the graphene layers are oriented away from horizontal and towards a vertical ordering, the nanoscale spaces developed underneath the droplet due to the interlayer spacing weakens the net attraction, *i.e.*, adhesive forces, resulting in a hydrophobic surface. Since the cohesive interactions between water molecules remain invariant for different petal orientations, the wettability of the surface is driven by the net attractive energies (U_{H_2O-C}) due to adhesive forces between the

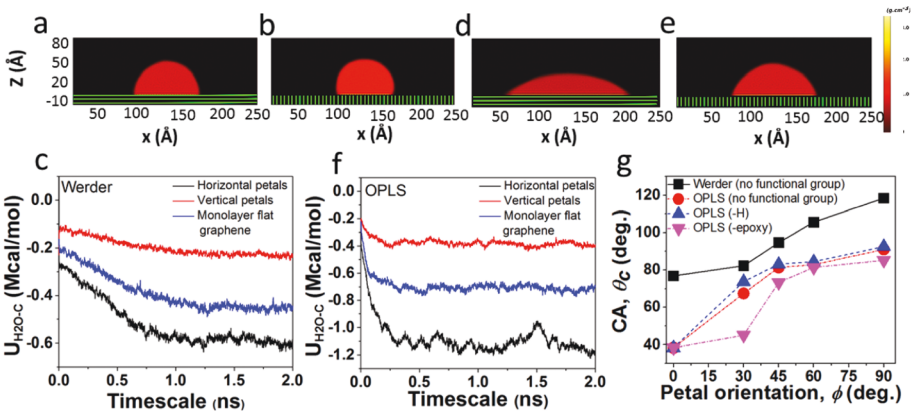

Fig. 3 MD simulations of the CA on IPG with horizontally and vertically aligned flakes. (a & b) Average mass density profile projected over the y–z plane of the equilibrated water droplet on horizontally and vertically oriented graphene respectively using Werder parameters. (c) Transient evolution and convergence of the water–graphene interaction energy using Werder parameters. (d & e) Average mass density profile projected over the y–z plane of an equilibrated water droplet on horizontally and vertically oriented graphene respectively using OPLS parameters. (f) Transient evolution and convergence of the water–graphene interaction energy using OPLS parameters. (g) Calculated contact angle of the droplet on the graphitic substrate for different graphene petal orientations (ϕ). Black squares are Werder potential parameters without any functional groups attached. Red circles are OPLS potential parameters without any functional groups attached. Blue triangles are OPLS potential parameters with hydrogen (–H) terminated edge atoms. Pink triangles are OPLS potential parameters with epoxy terminated graphene edge atoms.

droplet and substrate for the horizontal, vertical and intermediate configurations. Correspondingly, we observe a shift in θ_c from 76.87° to 118.5° when ϕ increases from 0° to 90° as illustrated in Fig. 3g (data shown with solid black squares).

CA values for water on graphene and graphite surfaces in the literature are inconclusive. For a given pair of liquid and solid substrate, several values of CAs can be obtained due to the intrinsic chemical heterogeneity and roughness of the solid substrate.[33,35] Furthermore, it was recently shown by Li *et al.*[18] that adsorption of airborne contaminants like hydrocarbons directly influences the wetting CA, while uncontaminated graphene is more hydrophilic than previously thought. Since the Werder parameters were optimized to reproduce the macroscopic CA of water droplet on a contaminated graphite sample (θ_c = 86°), the model implicitly includes some of the effects of contaminants.[29] In order to eliminate the effects of adsorbed contaminants, we performed additional simulations with the water–graphene interaction parameters derived from the Optimized Potential for Liquid Simulations-All Atoms (OPLS-AA) force field.[36] Fig. 3d–f reveal the changes in CA due to horizontal and vertical orientations of graphene petals and the corresponding convergence of water–graphene interaction energy. Similar to earlier predictions, U_{H_2O-C} for horizontally oriented graphene assumes a value ($\cong$–1.1 Mcal mol^{-1}) significantly more negative compared to the vertically oriented configuration ($\cong$–0.35 Mcal mol^{-1}). Correspondingly, as ϕ increases from 0° to 90° for bare graphene surfaces, θ_c also increases from 38.36° to 91.12° (Fig. 3g). This result confirms that the orientation of the graphene flakes has a direct influence on the U_{H_2O-C}, thus impacting CA and wettability.

The dangling bonds on the edges of the vertically oriented graphene in our model are highly reactive, and experimental evidence (heat loss and mass loss shown in Fig. S3 in ESI†) confirms the presence of functional groups. To understand the role of these functional groups, we performed additional simulations of two idealized cases: (i) all edge atoms of the graphene are hydrogen (–H) terminated, (ii) all the edge atoms of the graphene are epoxy terminated, each at 5 different graphene petal orientations (ϕ = 0°, 30°, 45°, 60°, and 90°). The epoxy terminated graphene sheets are more hydrophilic compared to the –H terminated sheets due to polar nature of the C–O bonds (Fig. 3g). This interaction increases the negative interaction energy (U_{H_2O-C}), due to stronger adhesive forces that enable surface wetting characteristics. Although there exist quantitative differences between the experimental and computational predictions of θ_c, we can clearly see that θ_c increases with ϕ in all of the cases considered. We attribute the mismatch in θ_c to the microscopic patterns (Fig. 1d & f) resulting from laser processing, which were absent in idealized simulations. Nevertheless, these results provide strong evidence that merely changing the orientation of the underlying graphene flakes induces hydrophobicity.

Finally, we present the simplicity and versatility of using DPLW to selectively pattern distinct superhydrophobic regions on IPG on an arbitrary surface to form distinct hydrophilic and hydrophobic regions on the same surface. The hydrophilic IPG regions were not treated with the laser while the hydrophobic regions were treated with the laser set with an energy density of 100 mJ cm^{-2} (Fig. 4). The wetting properties of these regions were analyzed within a FESEM where the chamber pressure, humidity, and temperature were altered in a controlled fashion (Fig. 4b–e). Initial water droplet formation could be observed on the hydrophilic regions when the chamber humidity was set to ~100%, the pressure at 640 Pa, and the temperature to 1.1 °C (Fig. 4b). Large water droplet

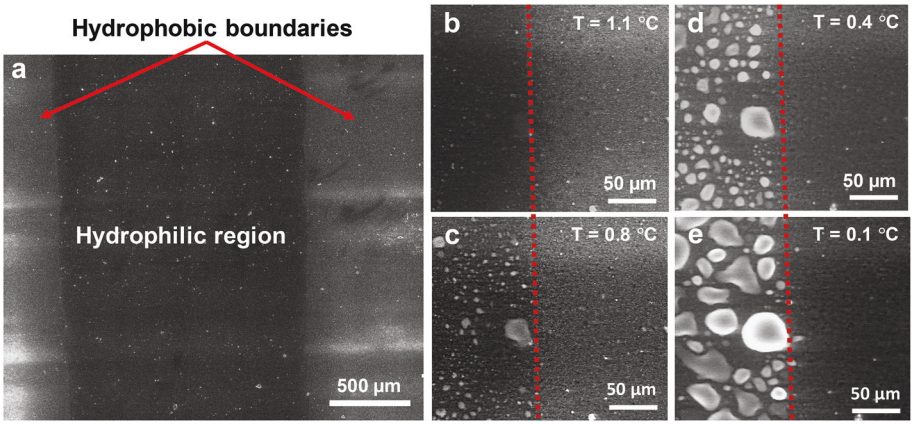

Fig. 4 FESEM images of a graphene hydrophilic/super-hydrophobic region formed using laser patterning and water droplet manipulation in the design. (a) Overall view of the distinctly treated IPG showing a hydrophilic region (darker region with width of ~1.5 mm) without laser processing confined by two superhydrophobic regions (lighter regions) treated with laser at an energy density of 100 mJ × cm^{-2}. (b–e) Water condensation experiments conducted within the FESEM operated in environmental mode (ESEM) display micrographs that capture the boundary (dotted red line) between the hydrophilic region (area the left of the red line) and the laser treated or hydrophobic region (region to the right of the dotted red line). As noted on the micrographs the humidity (*H*) and pressure (*P*) were held constant at approximately 100% and 640 Pa while the temperature (*T*) was varied from 1.1 °C to 0.1 °C. Water droplet formation begins to appear on the surface of the hydrophilic region of the IPG as the temperature is decreased to 0.8 °C and increases in magnitude as the temperature is dropped further to 0.4 °C and 0.1 °C.

formation gradually occurred as the chamber temperature was reduced from 1.1 °C to 0.8 °C, 0.4 °C, and 0.1 °C (Fig. 4c–e). ESI Video 1† demonstrates how water droplets distinctly form on a region of IPG treated with DPLW while not forming on an untreated region.

Conclusions

In summary, we have demonstrated a simple and scalable manufacturing method to produce large-scale 3D nanostructured graphene surface features that enable multifunctional properties: hydrophobic-superhydrophobic surface tunability, high electrical conductivity, and mechanical flexibility. In particular, this report demonstrates that the wettability of inkjet-printed graphene can be tuned *via* UV-laser irradiation. Molecular dynamics simulations confirm that the nanoscale vertical arrangement of the IPG after laser processing facilitates the induced superhydrophobicity. This modeling elucidates the relationship between nanoscale patterning and hydrophobicity—as most hydrophobicity studies focus on the relationship between microscale patterning and hydrophobicity. However, this work is a first step to explain the physiochemical underpinnings behind the connection of IPG surface morphology and chemical functionalization with hydrophobicity. Further research should be performed to further elucidate the association between both nano and micro IPG surface features as well as superficial chemical groups with regards to the resultant hydrophobicity.

The ability to selectively pattern superhydrophobic areas of hydrophilic IPG presents a material platform that could enable a wide range of emerging technologies such as self-cleaning chemical/biological sensors, flexible electronics, open microfluidics, and drag reduction and/or de-icing surfaces.[37–39] Also, the ability to selectively pattern superhydrophobic areas of hydrophilic IPG presents a potential scalable process that does not require the use of costly vacuum or cleanroom associated equipment such as lithographic patterning, metal evaporation, plasma treatment, and chemical vapor deposition.[40] Finally, the DPLW processing could also be coupled with high resolution graphene printing techniques such as inkjet maskless lithography[11] to create high resolution patterned graphene circuits on disposable substrates for electrochemical sensing applications[8,10,41] or to create flexible cell scaffolds/conduits for stem cell differentiation *via* electrical stimulation.[9] Rapid-pulse laser processing could also be potentially used to selectively anneal/sinter other thin film materials printed on chemically/thermally sensitive substrates including thermoelectric nanowires printed on polyimide for flexible thermoelectric energy harvesting.[42]

Methods

Inkjet-printing of graphene and post-print laser processing

Printable graphene ink, formulated following our previous recipes,[8] was loaded into the printer cartridge (10 pL nominal drop volume nozzle) of a Fujifilm Dmatix materials inkjet printer (DMP2800). Graphene writing parameters (such as waveform, temperature, viscosity of ink, drop spacing *etc*.) were used as optimized before,[8] on silicon as well as the polyimide substrates. The thermal annealing was performed (on graphene on silicon/oxide substrates) using a furnace with forming gas flow. Samples were annealed for 1 hour at 700 °C, 800 °C, 900 °C, and 1000 °C. The laser irradiation was performed on IPG on polyimide (25 μm thick) using a Nd:YAG pulsed laser

(3^{rd} harmonic at 355 nm and 15 ns pulse width) and the sample was exposed to the laser beam using an x–y translator.

Sheet resistance measurements

A Jandel Multi Height Probe with RM3000 Test unit was used for room temperature four-probe sheet resistance measurements. The measurements were done at five different areas on each sample and the mean value was reported.

Scanning electron microscope (SEM) and environmental scanning electron microscopy (ESEM) imaging

A Field-Emission Scanning Electron Microscope (FE-SEM) [FEI Quanta 250] was used for capturing the high resolution static images. The same microscope, but operating in the environmental operational mode (controlling the temperature and water vapor pressure inside the column) was used for water condensation experiments. Secondary electron (SE) mode with 10 kV accelerating voltage and a working distance of ~10 mm was used to capture the images. The *in situ* microscale wettability evolution experiments were perfomed on the unannealed and pulse-laser annealed IPG (laser energy density 100 mJ cm^{-2}) surfaces. A variable pressure (chamber pressure was varied between 400 Pa and 655 Pa), relative chamber humidity (between 61% and 100%) and variable temperature of the SEM sample stage (between 0.1 °C to 2.0 °C) with a FEI Quanta 250 FE-SEM were used for the environmental wetting test. The IPG with pulse laser treatment showed clear spherical droplet formation (Fig. 4 and ESI Video 1†).

Water contact angle measurements

The water contact angle was measured from the tangent angle formed at the three-phase contact of droplets captured by an in-house telescope-goniometer set up. For each sample, the measurements were made at three randomly chosen locations on the sample surface, and two independent drop shape analysis methods were used for each measurement: a general method to measure the contact angle by using the Dropsnak plugin of imageJ software with a piecewise polynomial fit (Axisymmetric Drop Shape Analysis (ADSA) method) and a $\theta/2$ method (where the liquid drop is assumed to be part of a sphere, by measuing the drop diameter and the height of the apex, the contact angle was calculated based on the following equation).

$$\frac{\theta}{2} = \tan^{-1}\left(\frac{h}{d}\right)$$

The reported contact angle is the average of the measured contact angle over three distinct samples. For each droplet, a 3 μL volume of water (DI water, resistivity ~18.3 MΩ cm) was used to avoid gravity-induced droplet-size alteration, side-view images were captured using a microscope attached to a camera, and the measurements performed at ambient conditions.

MD simulation

The interlayer spacing between the graphene sheets were maintained at 3.4 Å in all the cases considered. The interaction between the water molecules were modeled using the rigid extended simple-point-charge model (SPC/E) which considers the columbic interaction due to the partial charges on O ($-0.8476e$) and H ($+0.4238e$) atoms in addition to the 12–6 Lennard Jones (LJ) potential with σ_{O-O} = 3.166 Å and ε_{O-O} = 0.1553 kcal mol^{-1}. The interaction between the water molecules and the substrate atoms were also modeled using LJ potential. The Werder parameters used were σ_{C-O} = 3.190 Å and ε_{C-O} = 0.0950 kcal mol^{-1}. The parameters derived from OPLS force field were σ_{C-O} = 3.352 Å and ε_{C-O} = 0.1042 kcal mol^{-1}. The cutoff distance for the water–water interaction was 10 Å and 20 Å for the water–substrate interaction, to ensure accurate estimates of CA and interaction energies. The interaction between the functional groups and water molecules were also described by LJ potential with parameters derived from OPLS force field. For –H terminated case, σ_{H-O} = 2.768 Å and ε_{H-O} = 0.0682 kcal mol^{-1}. Due to the polar nature of the epoxy groups we consider the Columbic interaction due to the partial charges on C ($+0.4238e$) and O ($-0.8476e$) constituting the C–O bond. σ_{CT-O} = 3.3288 Å, ε_{CT-O} = 0.1012 kcal mol^{-1} and σ_{OT-O} = 3.0300 Å, ε_{OT-O} = 0.1474 kcal mol^{-1} where CT and OT represent the carbon and oxygen atoms of the C–O bond in the epoxy group. We initialized the simulation by arranging the water molecules in a periodic cubic ice structure and equilibrate the system at 26.85 °C (300 K) under NVT ensemble using the Nosé–Hoover thermostat until the interaction energy between the water droplet and substrate converges (see ESI† for more details). We sampled the data for the CA calculation after 2 ns when the system was well equilibrated. All the simulations were performed with Large-Scale Atomic/Molecular Massively Parallel Simulator (LAMMPS, http://lammps.sandia.gov).[43] More details regarding MD simulation methods are reported in the ESI†.

Conflicts of interest

There are no conflicts to declare.

Acknowledgements

J. C. C gratefully acknowledges the financial support by the National Science Foundation under grant number CBET-1706994, the USDA National Institute of Food and Agriculture, U.S. Department of Agriculture, under award number 2016-67021-25038 and project accession number 11901762, the Roy J. Carver Charitable Trust Foundation under award number 15-4615, as well as by the Iowa State University College of Engineering and Department of Mechanical Engineering. G. B. acknowledges research funding from the National Science Foundation (NSF) grant no. CMMI-1404938 and High Performance Computing HPC@ISU equipment at Iowa State University, some of which has been purchased through NSF funding MRI grant no. CNS 1229081 and CRI grant no. 1205413. J. C. C. and S. R. D. Special thanks to

Dr Daniel Attinger of Mechanical Engineering Department at Iowa State University and Dr Christophe Frankiewicz of Materials Science and Engineering Department at Iowa State University for providing experimental facility and measurement protocols respectively for contact angle measurements.

Notes and references

1 R. E. Sousa, C. M. Costa and S. Lanceros-Méndez, *ChemSusChem*, 2015, **8**, 3539–3555.
2 P. H. Lau, K. Takei, C. Wang, Y. Ju, J. Kim, Z. Yu, T. Takahashi, G. Cho and A. Javey, *Nano Lett.*, 2013, **13**, 3864–3869.
3 S.-M. Lee, R. Biswas, W. Li, D. Kang, L. Chan and J. Yoon, *ACS Nano*, 2014, **8**, 10507–10516.
4 J. Song and H. Zeng, *Angew. Chem., Int. Ed.*, 2015, **54**, 9760–9774.
5 S. Yao and Y. Zhu, *Nanoscale*, 2014, **6**, 2345–2352.
6 E. B. Secor and M. C. Hersam, *J. Phys. Chem. Lett.*, 2015, **6**, 620–626.
7 E. B. Secor, T. Z. Gao, A. E. Islam, R. Rao, S. G. Wallace, J. Zhu, K. W. Putz, B. Maruyama and M. C. Hersam, *Chem. Mater.*, 2017, **29**, 2332–2340.
8 S. R. Das, Q. Nian, A. A. Cargill, J. A. Hondred, S. Ding, M. Saei, G. J. Cheng and J. C. Claussen, *Nanoscale*, 2016, **8**, 15870–15879.
9 S. R. Das, M. Uz, S. Ding, M. T. Lentner, J. A. Hondred, A. A. Cargill, D. S. Sakaguchi, S. Mallapragada and J. C. Claussen, *Adv. Healthcare Mater.*, 2017, **6**, 1601087.
10 Q. He, S. R. Das, N. T. Garland, D. Jing, J. A. Hondred, A. A. Cargill, S. Ding, C. Karunakaran and J. C. Claussen, *ACS Appl. Mater. Interfaces*, 2017, **9**, 12719–12727.
11 J. A. Hondred, L. R. Stromberg, C. L. Mosher and J. C. Claussen, *ACS Nano*, 2017, **11**, 9836–9845.
12 E. B. Secor, B. Y. Ahn, T. Z. Gao, J. A. Lewis and M. C. Hersam, *Adv. Mater.*, 2015, **27**, 6683–6688.
13 E. B. Secor, P. L. Prabhumirashi, K. Puntambekar, M. L. Geier and M. C. Hersam, *J. Phys. Chem. Lett.*, 2013, **4**, 1347–1351.
14 F. Torrisi, T. Hasan, W. Wu, Z. Sun, A. Lombardo, T. S. Kulmala, G.-W. Hsieh, S. Jung, F. Bonaccorso, P. J. Paul, D. Chu and A. C. Ferrari, *ACS Nano*, 2012, **6**, 2992–3006.
15 H. Sojoudi, M. Wang, N. Boscher, G. McKinley and K. Gleason, *Soft Matter*, 2016, **12**, 1938–1963.
16 C.-H. Xue, Y.-R. Li, P. Zhang, J.-Z. Ma and S.-T. Jia, *ACS Appl. Mater. Interfaces*, 2014, **6**, 10153–10161.
17 J. Rafiee, X. Mi, H. Gullapalli, A. V. Thomas, F. Yavari, Y. Shi, P. M. Ajayan and N. A. Koratkar, *Nat. Mater.*, 2012, **11**, 217–222.
18 Z. Li, Y. Wang, A. Kozbial, G. Shenoy, F. Zhou, R. McGinley, P. Ireland, B. Morganstein, A. Kunkel and S. P. Surwade, *Nat. Mater.*, 2013, **12**, 925–931.
19 C.-J. Shih, Q. H. Wang, S. Lin, K.-C. Park, Z. Jin, M. S. Strano and D. Blankschtein, *Phys. Rev. Lett.*, 2012, **109**, 176101.
20 J. Driskill, D. Vanzo, D. Bratko and A. Luzar, *J. Chem. Phys.*, 2014, **141**, 18C517.
21 Y. J. Shin, Y. Wang, H. Huang, G. Kalon, A. T. S. Wee, Z. Shen, C. S. Bhatia and H. Yang, *Langmuir*, 2010, **26**, 3798–3802.
22 F. Taherian, V. Marcon, N. F. van der Vegt and F. d. r. Leroy, *Langmuir*, 2013, **29**, 1457–1465.
23 F. Perrozzi, S. Croce, E. Treossi, V. Palermo, S. Santucci, G. Fioravanti and L. Ottaviano, *Carbon*, 2014, **77**, 473–480.
24 I. K. Moon, J. Lee, R. S. Ruoff and H. Lee, *Nat. Commun.*, 2010, **1**, 73.
25 V. V. Shunaev and O. E. Glukhova, *J. Phys. Chem. C*, 2016, **120**, 4145–4149.
26 L. Bocquet and E. Lauga, *Nat. Mater.*, 2011, **10**, 334–337.
27 Y. Baskin and L. Meyer, *Phys. Rev.*, 1955, **100**, 544–544.
28 H. Berendsen, J. Grigera and T. Straatsma, *J. Phys. Chem.*, 1987, **91**, 6269–6271.
29 T. Werder, J. H. Walther, R. Jaffe, T. Halicioglu and P. Koumoutsakos, *J. Phys. Chem. B*, 2003, **107**, 1345–1352.
30 M. J. De Ruijter, T. Blake and J. De Coninck, *Langmuir*, 1999, **15**, 7836–7847.
31 T. Ingebrigtsen and S. Toxvaerd, *J. Phys. Chem. C*, 2007, **111**, 8518–8523.
32 S. H. Park, M. A. Carignano, R. J. Nap and I. Szleifer, *Soft Matter*, 2010, **6**, 1644–1654.
33 F. d. r. Leroy and F. Müller-Plathe, *Langmuir*, 2015, **31**, 8335–8345.
34 T. Ondarçuhu, V. Thomas, M. Nuñez, E. Dujardin, A. Rahman, C. T. Black and A. Checco, *Sci. Rep.*, 2016, **6**, 24237.
35 L. Gao and T. J. McCarthy, *Langmuir*, 2009, **25**, 14105–14115.
36 W. L. Jorgensen, D. S. Maxwell and J. Tirado-Rives, *J. Am. Chem. Soc.*, 1996, **118**, 11225–11236.
37 R. Truesdell, A. Mammoli, P. Vorobieff, F. van Swol and C. J. Brinker, *Phys. Rev. Lett.*, 2006, **97**, 044504.
38 D. V. Ta, A. Dunn, T. J. Wasley, R. W. Kay, J. Stringer, P. J. Smith, C. Connaughton and J. D. Shephard, *Appl. Surf. Sci.*, 2015, **357**, 248–254.
39 X. Zhang, F. Shi, J. Niu, Y. Jiang and Z. Wang, *J. Mater. Chem.*, 2008, **18**, 621–633.
40 Y. Y. Yan, N. Gao and W. Barthlott, *Adv. Colloid Interface Sci.*, 2011, **169**, 80–105.
41 S. L. Burrs, M. Bhargava, R. Sidhu, J. Kiernan-Lewis, C. Gomes, J. C. Claussen and E. S. McLamore, *Biosens. Bioelectron.*, 2016, **85**, 479–487.
42 B. Chen, S. R. Das, W. Zheng, B. Zhu, B. Xu, S. Hong, C. Sun, X. Wang, Y. Wu and J. C. Claussen, *Adv. Electron. Mater.*, 2017, **3**, 1600524.
43 S. Plimpton, *J. Comput. Phys.*, 1995, **117**, 1–19.